The Influence of Sheet Metal Anisotropy on Laser Forming Process (101)

Peng Cheng and Y. Lawrence Yao, Department of Mechanical Engineering, Columbia University, New York, NY 10027, USA

ABSTRACT

Cold rolled sheet metal often used in laser forming exhibits anisotropic properties, which are mostly caused by preferred orientations of grains developed during the severe plastic deformation. In present study, the textures of cold-rolled mild steel sheets are characterized and the influence of the plastic anisotropy on laser forming process is investigated. Deformation textures are measured in terms of pole figures and orientation distribution function (ODF) plots obtained through electron backscatter diffraction (EBSD). The anisotropy index (*R*-value) of the material with different rolling reductions is obtained by uniaxial tensile tests. Both are compared and agree with the texture development theory. Effects of the plastic anisotropy on bending deformation during the laser forming process are investigated experimentally and numerically. Various conditions such as sheet thickness reductions, scanning speed and laser power are considered and results are discussed. The simulation results are consistent with the experimental observations.

1. INTRODUCTION

Laser forming is a flexible rapid prototyping and low-volume manufacturing process, which uses laser-induced thermal distortion to shape sheet metal parts without tooling or external forces. Understanding various aspects of laser forming is a challenging problem of considerable theoretical and practical interest. Studies of material property effects on the laser forming process were reported, such as influence of strain hardening [1] and strain rate [2]. The effects of anisotropy on the laser forming process, however, have not been studied in detail, while most sheet metal materials used in the laser forming are cold rolled.

Anisotropy includes elastic and plastic anisotropy. In cold rolled sheet, elastic deformation is much smaller compared with the plastic deformation, so only the anisotropic plasticity is normally considered [3]. The type of plastic anisotropy usually desired in sheet metal forming is that in which the sheet is isotropic in the plane and has an increased strength in the thickness direction, which is normally referred to as normal anisotropy. More often, however, the type of plastic anisotropy is characterized by different strengths in different directions in the plane of the sheet, which is called planar anisotropy. This is simply because of the different amount of deformation along the rolling and other directions in the plane. The plastic anisotropy is commonly characterized by *R*-values, which will be explained in more details in late sections. In this study, the planar plastic anisotropy is simply referred to as anisotropy.

The primary source of such plastic anisotropy comes from the texture or the preferred crystallographic orientations of the grains as a result of cold rolling. The plastic anisotropic properties of sheet metals have generally been investigated independently by two approaches [4]. The first one is to develop various macroscopic yield functions from a phenomenological viewpoint [5,6]. The second approach is to develop polycrystal models based on the constitutive behavior of crystalline slip in single crystals [7,8]. Although the studies on anisotropy have been investigated both macroscopically and microscopically, the effect of anisotropy on laser forming has not been investigated specifically.

In present study, the effect of anisotropy exhibited in cold-rolled mild steel sheets on laser forming process is investigated. To better characterize the anisotropy, pole figures and orientation distribution function (ODF) plots of steel sheet were obtained by electron backscatter diffraction (EBSD) and compared with those predicted by deformation texture theories. *R*-values were measured and compared with those predicted by theories. Effect of such anisotropy on laser forming under various conditions, such as different sheet thickness reductions, scanning speed and laser power were experimentally and numerically investigated.

2. BACKGROUND

2.1 Deformation textures in *BCC* sheet metals

Sheet texture is described by the Miller index notation (*hkl*)[*uvw*], in which the crystallographic plane (*hkl*) is roughly parallel to the sheet surface, and the direction [*uvw*] in that plane is roughly parallel to the rolling direction (*RD*). Various types of textures are possible to form in cold rolled sheet metal depending on material type and processing condition. Both experimental and simulation results have shown that four texture components, {001}<110>, {112}<110>, {111}<112> and {111}<110>, are possible in cold rolled *BCC* metals of initially random textures [9]. Which texture components in *BCC* metals are present and more dominant also depends on process condition [10]. For instance, when rolling reduction is moderate, (i.e. < 70%), {001}<110> and {112}<110> are the dominant components on the α -fiber, that is, <110> is parallel along *RD,* and one sees a weak preference of {111}<112> on the γ -fiber, that is, {111} is parallel along the normal direction (*ND*) of the sheet. For large rolling reduction (i.e. > 70%) the maximum on the α-fiber is shifted to {112}<110> and that on the γ -fiber from {111}<112> to {111}<110>.

The texture type developed in plastic deformation of polycrystals is usually controlled by crystallographic slip in the individual grains. It is the result of the rotation of slip systems in grains during plastic deformation. Such rotations are along particular directions. For instance, in the case of tension, the slip direction vector rotates gradually towards the tensile direction and the slip plane normal rotates away from the tensile axis. This characteristic orientation change is the major reason of rolling texture development and can be explained by Schmid and Taylor theory [11]. That is, in the tensile case, during the decrease of the angle between the tensile axis and slip direction, the Schmid factor decrease until another slip system with higher Schmid factor is activated instead. Then the slip direction of that newly activated slip system rotates towards the tensile axis. This process ends when it reaches a stable orientation. For the tensile case, [112] and [110] are the main stable orientations for *FCC* and *BCC* metals, respectively. Due to the multiple systems of slip for the *BCC* metals, there are multiple stable orientations for the *BCC* metals. This also explains why multiple components of texture occur in *BCC* metals.

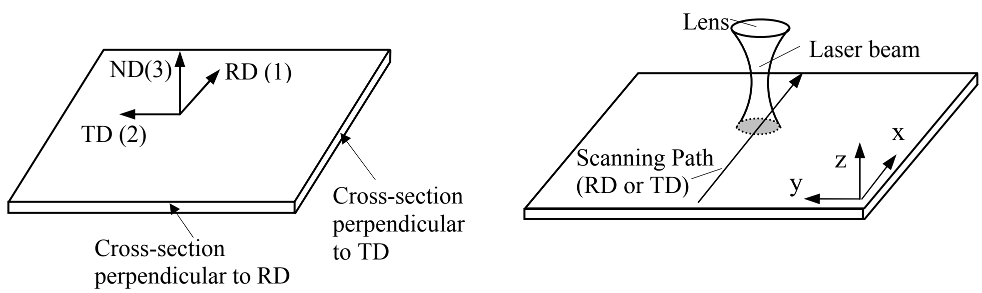

(a) (b)

Figure 1. (a) Rolled-sheet coordinate system and terminology: *RD*: rolling direction, *TD*: transverse direction, and *ND*: normal direction; and (b) Schematic laser forming system (scanning path along *RD* or *TD*).

2.2 Theoretical method to predict texture formation

To quantitatively predict the development of textures, several models were developed. The most widely applied model to predict the texture development is Taylor-like model [12], which assumes that the strain of the individual crystallites is equal to the strain of the polycrystalline aggregate and are therefore called the "Full Constraint" (FC) model. Another assumption of the FC model is the activation of at least five slip systems in each crystallite so that all five independent components of a general strain tensor may be accommodated. In Taylor's model, the work increment done during the tension process in terms of the macroscopic stress σ_p and the strain increments $d\varepsilon$ equals to the internal work done by the critical shear stress $\tau_0^{(r)}$ and shear strain increments $d\gamma^{(r)}$ in the *r*-th slip system (r=1,2,…5).

$$\sigma_p d\varepsilon = \sum_{r=1}^{5} \tau_0{}^{(r)} d\gamma^{(r)} \tag{1}$$

Assuming the critical shear stress $\tau_0^{(r)}$ is the same for all slip systems and equal to τ_0. The Taylor factor can be defined as

$$M = \frac{\sigma_p}{\tau_0} = \frac{\sum_{r=1}^{5} d\gamma^{(r)}}{d\varepsilon} \tag{2}$$

Taylor factor M can be compared with the reciprocal of the Schmid factor. Combinations of slip systems with the minimum Taylor's factor will be the active slip systems in the plastic deformation.

Deformation textures calculated according to the Taylor model are in fairly good qualitative agreement with the observed ones. However, some discrepancies exist when it was applied in large reduction cases. "Relaxed Constraint" (RC) models were developed based on the Taylor model to describe texture development in large deformation [7]. Unlike the Taylor approach where strain compatibility is strictly prescribed, in the RC models partial constraints are imposed on the basis of mixed boundary conditions: some components of strain and the others of stress are presumed given. For cold rolling with large reduction, the RC models are more accurate to predict the texture development compared with the FC model. Two kinds of RC models were applied: one is the lath model with ε_{13} relaxed, and the other is the pancake model with both ε_{13} and ε_{23} relaxed, where 1 represents the rolling, 2 the transverse, and 3 the normal direction (Fig. 1a). Kocks, et al. [9] pointed out that for simulating low reductions, the FC Taylor model is preferred. For describing intermediate reductions, the lath model, and for large reductions, the pancake model is more suitable.

3. EXPERIMENTAL AND SIMULATION CONDITIONS

3.1 Texture measurement

Texture measurements of AISI 1010 cold rolled steel sheets 1.4mm and 0.89mm thick were carried out using electron back-scatter diffraction (EBSD). A series of typical scans were recorded with a step size of $3\mu m$ and consisted of 3000-6000 indexed points. Four incomplete pole figures {100}, {110}, {111} and {112} were measured in the rolling plane (*RD-TD* plane where *TD* stands for transverse direction). Three-dimensional orientation distribution functions (ODFs) $f(g)$ were calculated by using the spherical harmonics [13]. The ODFs are represented in three-dimensional Euler space in the range of $0^0 \le \varphi_1, \phi, \varphi_2 \le 90^0$ by way of iso-intensity contour lines in different sections with an Euler angle held constant. Grain structures in different cross-sections were observed by scanning electron microscope (SEM). Samples were polished and etched using 3% HNO_3 for 5 seconds for EBSD and 20 seconds for SEM.

3.2 Measurement of *R*-values

In accordance with the ASTM Standard E517 [14], the *R*-values of AISI 1010 cold rolled steel sheets 1.4mm and 0.89mm thick, were measured by uniaxial tensile tests on a material testing machine. The specimens were cut by a CNC machine with axes along the rolling direction (*RD*), transverse direction (*TD*) or 45^o to the rolling direction, corresponding the measurement of R_0, R_{45} and R_{90}, where the subscripts represent the angle to the rolling direction.

The specimens have gage length of 1.6" and width of 0.4". Due to the difficulty in measuring gage thickness changes with sufficient precision, an equivalent relationship is commonly used, based on length and width strain measurements:

$$R = \frac{\varepsilon_w}{\varepsilon_t} = \frac{\ln(w_i / w_f)}{\ln(l_f w_f / l_i w_i)} \tag{3}$$

where ε_w and ε_t are true strain in width and thickness directions of a specimen; w_i, w_f and l_i, l_f are initial and final gage width and length, respectively.

Measurement accuracy is improved as the strain is increased but within the necking limits. Strains of 10 to 20% are commonly utilized in determining the *R*-value of low carbon steels. In present study, approximate 15% plastic strain is utilized. The strain rate in the uniaxial tensile tests was taken to be 1.25×10^{-3}/s, which is within the range of the ASTM Standard ($< 8.33\times10^{-3}$ /s).

3.3 Laser forming experiments

The material is cold rolled AISI 1010 steel, and the workpiece size is 80 mm by 80 mm with thickness of 1.4 mm and 0.89 mm. Experiments of straight-line laser forming were carried out along *RD* and *TD*, respectively (Fig. 1b). The laser system used in the experiments is a PRC-1500 CO_2 laser, with a maximum output power of 1.5KW and power density distribution was TEM_{00}. In present study, various conditions such as different material reduction (corresponding to two different workpiece thickness levels), different scanning speed (from 50 mm/s to 90 mm/s), different laser power (from 600 w to 800 w) and number of scans (1 and 10) were applied. Laser beam diameter varied from 6 mm to 4 mm when the sample thickness changed from 1.4 mm to 0.89 mm. A coordinate measuring machine (CMM) is used to measure the bending angle at different positions along the scanning path. To enhance laser absorption by the workpiece, graphite coating is applied to the surface exposed to the laser.

3.4 Numerical simulation

In numerical simulation the laser forming process is modeled as a sequentially coupled thermal-mechanical process. In the thermal analysis, the transient conduction for a solid workpiece irradiated by a laser beam can be expressed in terms of temperature as:

$$\rho c_p \frac{\partial T}{\partial t} = \nabla \cdot (k \nabla T) \tag{4}$$

where ρ, c_p, k are the density, specific heat and thermal conductivity, respectively. At the heating surface, $\alpha_{abs} F \cdot \hat{n} = -\hat{n} \cdot (k \nabla T)$, where α_{abs} is the material's absorbency and $\hat{n}$ is the unit vector normal to the surface pointing to the solid. The heat flux due to the Gaussian laser power is expressed as

$$F = Q_{\max} \exp(-R_k R^2) \text{ and } Q_{\max} = P_{laser} R_k / \pi \tag{5}$$

where $Q_{\max}$ is the heat flux intensity of the laser beam, R is the distance to the laser beam center, R_k is the concentration coefficient, and P_{laser} is the laser power.

All the surfaces of workpiece subject to the convective heat flux that is $f = h(T - T_s)$, where h is the convective heat transfer coefficient, T is the surface temperature, and T_s is the surrounding temperature. The radiation heat flux is also considered at the heating surface which is $f_c = \varepsilon\sigma(T^4 - T_s^{\,4})$, where ε and σ are emissivity and Stefan-Boltzmann constant, respectively.

In the mechanical analysis, Hooke's law was used for elastic deformation, and for the plastic-deformation state, the flow rule is

$$d\varepsilon_{ij} = d\lambda \frac{\partial f}{\partial \sigma_{ij}} \tag{6}$$

where ε_{ij} is the strain tensor, σ_{ij} is the stress tensor, $d\lambda$ is the instantaneous, positive, varying, proportionality factor (plastic compliance), and $f = f(\sigma_{ij})$ is the yield function. For anisotropic analysis Hill's potential function is applied instead of Von Mises function. In sheet metal forming applications plane stress condition is generally assumed. Hill's yield criterion can be written as

$$(G+H)\sigma_{11}^{\;2} - 2H\sigma_{11}\sigma_{22} + (H+F)\sigma_{22}^{\;2} + 2N\tau_{12}^{\;2} = 1 \tag{7}$$

In a simple tension test performed in the rolling direction in the plane of the sheet, the incremental strain ratio can be written as

$$d\varepsilon_{11} : d\varepsilon_{22} : d\varepsilon_{33} = (G+H) : (-H) : (-G) \tag{8}$$

According to the definition of *R*-value (Eq. 3), it is obtained

$$\frac{H}{G} = \frac{d\varepsilon_{22}}{d\varepsilon_{33}} = R_0 \cdot \tag{9}$$

Similarly, for a simple tension test performed in the 90^0 and 45^0 to the rolling direction,

$$\frac{H}{F} = R_{90} \quad \text{and} \quad \frac{N}{G} = (\tfrac{1}{2} + R_{45})(1 + \frac{R_0}{R_{45}}) \tag{10}$$

Since the thermal and mechanical deformations are symmetric about the vertical plane containing the scanning path, only half of the plate is modeled in the numerical simulation. In numerical simulation, the main assumptions used are as follows. Plastic deformation generated heat is small as compared to energy input in laser forming so that it is negligible. During the entire laser forming process, no melting takes place. The symmetric plane is assumed to be adiabatic. ABAQUS was used to complement the numerical simulation. The same mesh model was used for the thermal and mechanical deformations. A 20-nodes brick element was used in the mechanical analysis because this kind of element has no shear locking and hourglass stiffness and is also suitable for bending-deformation-dominated processes such as laser forming. In order to remain compatible with the structural analysis, an element, DC3D20, is used in heat transfer analysis. A user subroutine of dflux was developed to model the heat source input from the Gaussian laser beam.

4. RESULTS AND DISCUSSION

4.1 Texture characterization

Figure 2a shows the four incomplete pole figures {100}, {110}, {111} and {112} of the cold-rolled steel sheet with thickness of 1.4 mm. The main texture components can be obtained from pole figures qualitatively. In the normal direction (*ND*), a stronger component of {111} and weaker components of {001} and {112} were seen. In the rolling direction (*RD*), a stronger <110> direction and weaker <001> and <112> directions were identified. Three major components of textures {111}<110>, {112}<110> and {001}<110> were therefore determined, while in the subsequent orientation distribution function (ODF) plots more exact components were obtained.

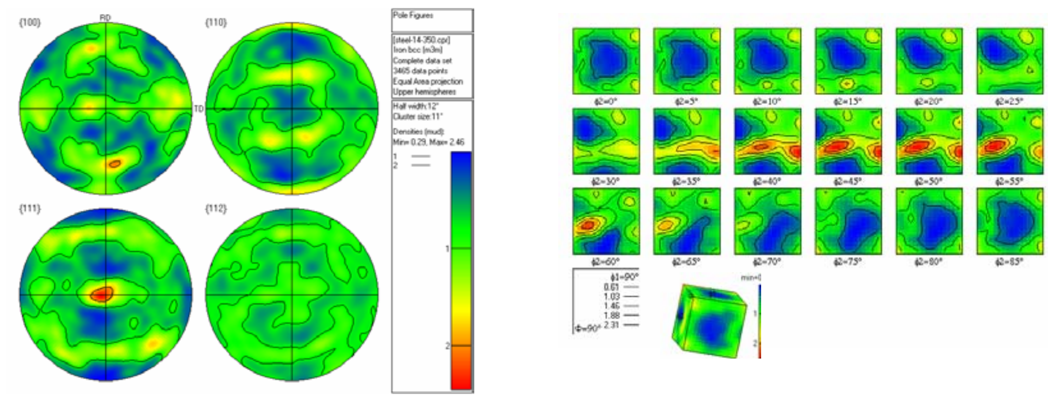

(a) (b)

Figure 2. (a) {001}, {110}, {111} and {112} pole figures of AISI 1010 cold-rolled steel sheet 1.4 mm thick; and (b) orientation distribution functions (ODFs) of the same sample

Unless the texture of a material is very simple, it is very difficult to determine quantitatively from pole figures or inverse pole figures all the orientations present. ODF can fully describe a texture because it can be determined by mathematically representing the texture by spherical harmonics. Figure 2b shows ODF sections (with φ_2 increments from 0^o to 85^o) for the same material by EBSD. By transforming Euler angles to texture representation (*hkl*)[*uvw*], the major components of textures can be determined. The α-fiber textures are $(112)[1\bar{1}0]$ and $(001)[1\bar{1}0]$ and the γ-fiber textures are $(111)[0\bar{1}1]$ and $(111)[\bar{1}\bar{1}2]$. This observation is consistent with the texture development theory (Section 2a). That is, in lower reduction like this case (thickness of 1.4mm), {001}<110> and {112}<110> are the dominant components on the α-fiber (<110>//RD) and one sees a weak preference of {111}<112> on the γ-fiber ({111}//ND). {111}<110> is dominant because it belongs to both α-fiber and γ-fiber.

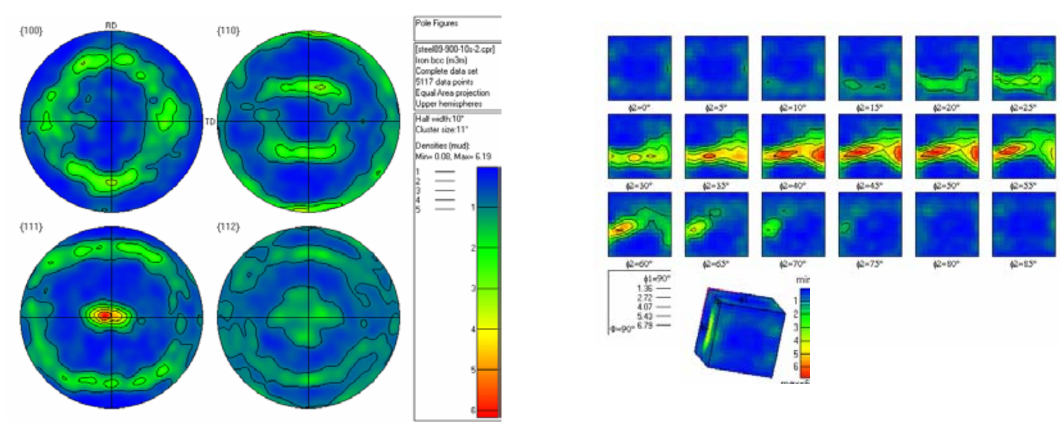

(a) (b)

Figure 3. (a) {001}, {110}, {111} and {112} pole figures of AISI 1010 cold-rolled steel sheet 0.89 mm thick; and (b) orientation distribution functions (ODFs) of the same sample

Figure 3a shows the {100}, {110}, {111} and {112} pole figures obtained from steel sheet 0.89 mm thick which represents larger rolling reduction. The obvious difference can be found in {100} pole figure compared with that of 1.4 mm steel sheet. {001} texture has disappeared and <110> is the major direction along the rolling direction. From ODFs on Figure 3b, the major components of textures are determined as α-fiber $(112)[1\bar{1}0]$ to $(111)[1\bar{1}0]$ and γ-fiber $(111)[0\bar{1}1]$. The change of texture components is consistent to the texture development theory. That is, when rolling reduction is higher, the maximum on the α-fiber is shifted to {112}<110> so that {001}<110> components can be neglected. In γ-fiber the components of textures shift from {111}<112> to {111}<110>.

The grain structure at different cross sections of the cold rolled sheet was observed by scanning electron microscopy (SEM). Figure 4 shows the grain structures in cross sections perpendicular to the *TD* and *RD* directions of the cold-rolled steel sheet with thickness of 1.4 mm, respectively. It can be seen that grains are substantially elongated in the rolling direction while no significant changes are seen along the transverse direction. This is due to the deformation characterization of the cold rolling process. In cold rolling plates and sheets with high width-to-thickness ratios, the width of the material remains essentially constant and the length of the material is substantially elongated during rolling.

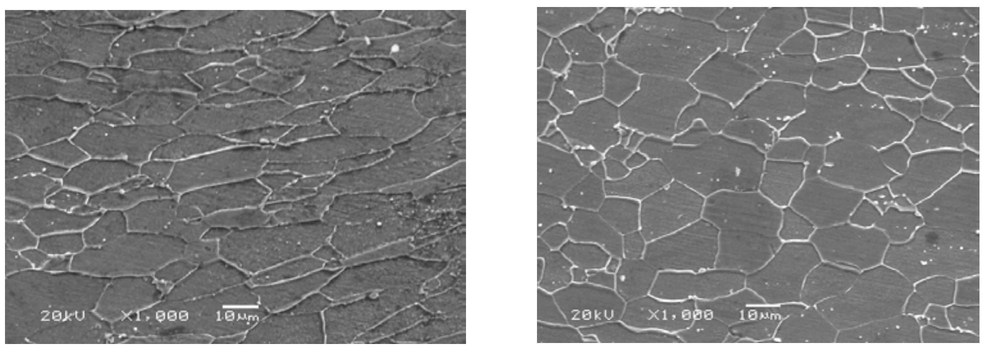

(a) (b)

Figure 4. SEM micrographs of grain structures of cold rolled AISI 1010 steel 1.4mm thick (x1000) (a) cross-section perpendicular to the transverse direction (*TD*); and (b) cross-section perpendicular to the rolling direction (*RD*).

4.2 Macro anisotropic properties, *R*-value and yield stress

Figure 5 shows *R*-values determined in tensile tests for two different sheet reductions and along three different angles to rolling direction. The pattern of *R*-values between the two reduction levels is somewhat similar but different in the following way. In the lower reduction case (thickness of 1.4mm), the *R*-value along the rolling direction (*RD*), R_0, is larger than that along the transverse direction (*TD*), R_{90}. While in the higher reduction case (thickness of 0.89mm), R_0 is slightly smaller than R_{90}. This result is consistent with theoretical predictions.

The prediction of *R*-values using the series expansion method is generally carried out within the framework of the Taylor's model. To improve the accuracy of predictions, "Relaxed Constraint" grain interaction models are employed [15]. The Taylor or full constraint (FC) model had been shown to be more accurate in prediction at lower reduction cases. While in higher reduction cases, the relaxed constraint (RC) model is more accurate due to the more accurate boundary conditions.

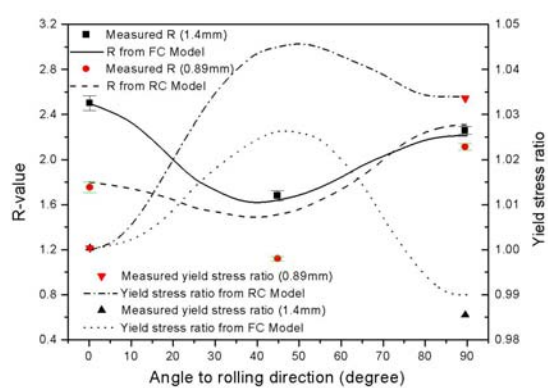

Figure 5. Comparison of *R*-values and yield stress ratio between measured value and theoretical prediction [15] for ASIS 1010 sheet metal of 1.4 mm thick and 0.89 mm thick

From Figure 5, a very good agreement can be seen for the lower reduction case (thickness =1.4mm), while for 0.89mm case, agreement is again seen for R_0 and R_{90} but some discrepancy between the measured and predicated values is seen for R_{45}. A likely reason for the discrepancy is as follows. It is known that the RC approach is appropriate for describing the deformation of aggregates of pancake-shaped grains. For cold-rolled low carbon steel, the elongated and flattened grains are mostly along the rolling direction. As a result, the predictions obtained from the RC model fit the experimental data somewhat better from 0 deg to 45 degrees. For angles above 45 degrees, the grains are no longer elongated along the tensile axis, so that the grain shape argument for using this model is not valid any more.

Figure 5 also compares yield stress ratio between indirectly measured values and theoretical predictions. The indirectly measured values are obtained by measured *R*-values and Hill's yield criterion . As expected, the prediction based on the FC model fits the lower reduction case closely and that based on the RC model fits the high reduction case closely.

4.3 Anisotropic effect on laser forming involving different material reductions

80 by 80 by 1.4 mm samples were scanned along either *RD* or *TD*. Figure 6a shows the experimental and numerical results of bending angles caused by the laser scanning and a reasonable agreement is seen. The experiments were repeated two to three times and the repeatability is shown in terms of error bars around the data points. Bending angles are measured at five equally spaced positions along the scanning direction. The difference between these five points is due to the so-called edge effects which had been thoroughly studied before. But there is obvious difference in bending angle between scanning along *RD* and *TD*. Since the flow stress in *TD* is smaller than that in *RD* (Fig. 5), the bending angle when scanned along *TD* is smaller than that when scanned along *RD* because it is well known that the plastic deformation perpendicular to the scanning direction is primarily responsible for the bending angle.

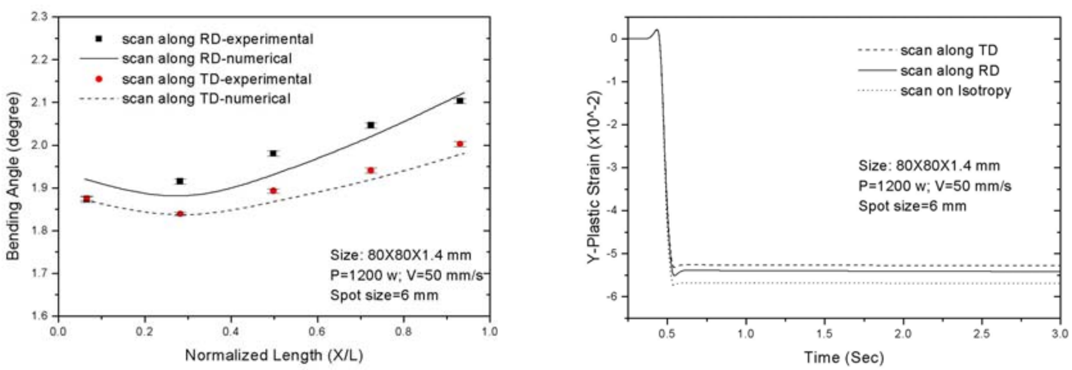

(a) (b)

Figure 6. (a) Numerical and experimental bending angles of 1.4 mm thick steel sheet with scanning along *RD* and *TD*, respectively; and (b) Simulated time history of plastic strain in the *y* direction, which is perpendicular to the scanning path (results on isotropic sheets also included).

To further illustrate the point, Figure 6b compares the simulated *y*-plastic strain (*y* is perpendicular to the scanning direction as shown in Fig. 1b) for scanning along *RD* and *TD*. As expected, it is smaller when scanned along *TD* than that along *RD*. Scanning on the same but hypothetically isotropic material is also superposed for comparison. The isotropic material is assumed to have *R*-values equal to 1 and the yield stress is 30% smaller than that of cold rolled sheet. The *y*-plastic strain of isotropic material is larger due to the smaller flow stress than that of the anisotropic material.

The bending angle difference of samples with thickness of 0.89 mm is quite different from that of samples with thickness of 1.4 mm. Since in this case the yield stress in *RD* is smaller than that of *TD* (Fig. 5), bending angle is smaller when scanning along *RD* than that of scanning along *TD*. This is consistent experimentally and numerically as shown in Figure 7a. Figure 7b illustrates results similar to that shown in Fig. 6b. In summery, difference of bending deformation exists when scanning along different directions in the anisotropic material used in this study.

With the rolling reduction of steel sheet increasing, the anisotropic effect on laser induced bending is more pronounced.

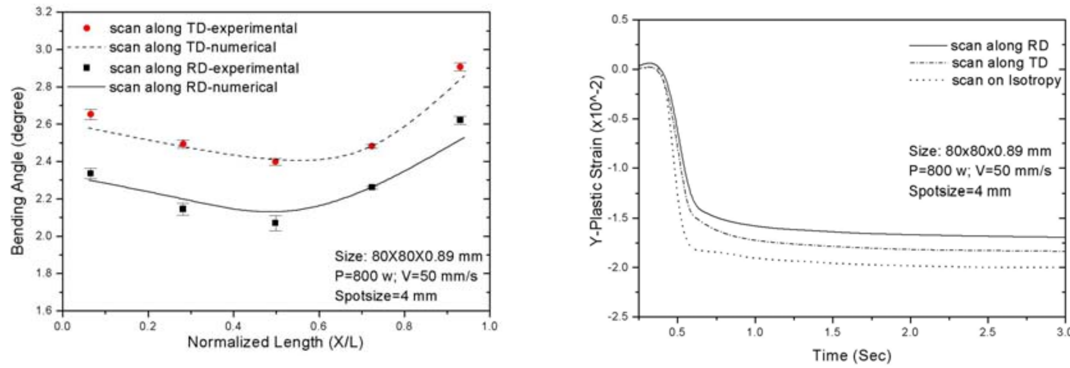

(a) (b)

Figure 7. (a) Numerical and experimental bending angles of 0.89 mm thick steel sheet with scanning along *RD* and *TD*, respectively; and (b) Simulated time history of plastic strain in the *y* direction, which is perpendicular to the scanning path (results on isotropic sheets also included).

4.4 Anisotropic effect under various scanning speeds

Influence of plastic anisotropy on laser forming deformation under various scanning speeds is investigated for the 0.89 mm thick case. Both experimental and numerical results are presented and show agreement. From Figure 8a, it can be seen that when the scanning speed increases while the laser power is kept constant, the average bending angle decreases whether it was scanned along *RD* or *TD*. This is obviously due to the decreased laser energy input per unit time, which causes decreased temperature rise. At the same time, increased speed increases strain rate which in turns causes increased flow stress.

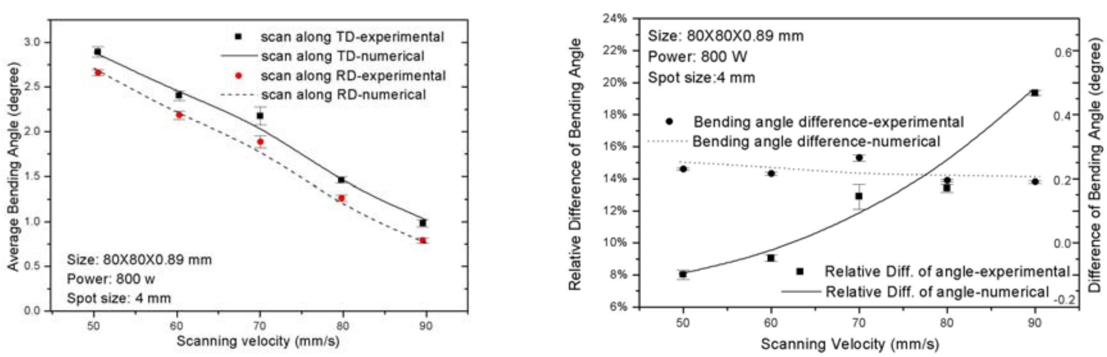

(a) (b)

Figure 8. (a) Bending angle; and (b) Differences of bending angle between scans along *RD* and *TD* (Constant laser power and varying speed)

However, the bending angle difference between scanning along *RD* or *TD* seems not to change with speed and remains more or less constant within the speed range investigated. Figure 8b shows the difference and relative difference of bending angles when scanning along *RD* or *TD* under different speeds. The almost constant difference confirms the above observation. The reason for that is, when scanning speed increases, the temperature drop and strain rate increase is almost the same when scanning with the same speed along *RD* or *TD* (Fig. 9). So the flow stress in *RD* and *TD* will increase by a similar amount and the difference of flow stress does not change much in the absolute sense. As a result, the absolute difference of bending angles almost does not change. But if comparing the relative difference of the bending angles, which is defined as the ratio of difference to average bending angles, a clear increasing trend with speed can be seen (Fig. 8b). This is because, although the difference of flow stress does not change much with speed, the relative difference increases since the average bending angle decrease with the increasing speed. From Figure 8b, it is seen the anisotropic effect increases from 8% to 19% when scanning speed increases from 50 mm/s to 90 mm/s.

Besides the explanation stated above, another possible reason for the increasing relative bending angle difference between scanning along *RD* and *TD* with speed is the effect of temperature change with speed on microstructure change. When scanning velocity is higher, the temperature rise is lower and time for the heated material to recrystallize or to neutralize the anisotropy effect is shorter. As a result, the anisotropy effect relative to the bending angle will increase with the scanning speed.

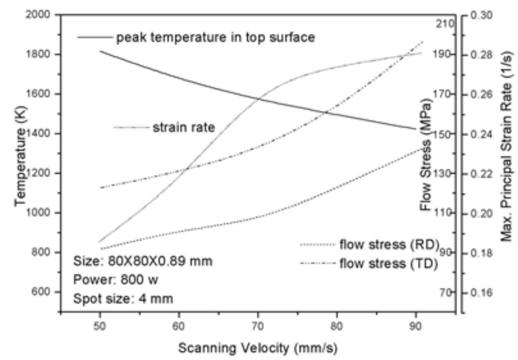

Figure 9. Simulated peak temperature strain rate, and yield stress when scanning along rolling direction and transverse direction

4.5 Anisotropy effect under condition of various laser powers

Experiments under condition of constant scanning speed and various laser powers have been investigated when scanning is carried out either along *RD* or *TD*. Since the scanning speed was kept constant, the effect of strain rate can be neglected. When laser power is higher, input heat energy and thus temperature rise is higher. As a result, flow stress decreased and bending angle increased with laser power increasing (Fig. 10a). Since the temperature and flow stress effect on the bending deformation is almost the same for scanning along *RD* or *TD*, the absolute difference bending angle does not change much with power (Fig. 10b). But again if the relative difference is calculated, it decreases from about 15% to 8% with power increase. This can be similarly explained as for the speed case. Higher temperature caused by the higher laser power allows the anisotropic material to more actively recrystallize while being formed, and thus negates part of the anisotropy effect. So when the laser power increases while keeping a constant scanning speed, the relative difference of bending angle between scanning along *RD* and *TD* will decrease. The trend shown in Figure 10b is consistent based on both experimental and numerical results.

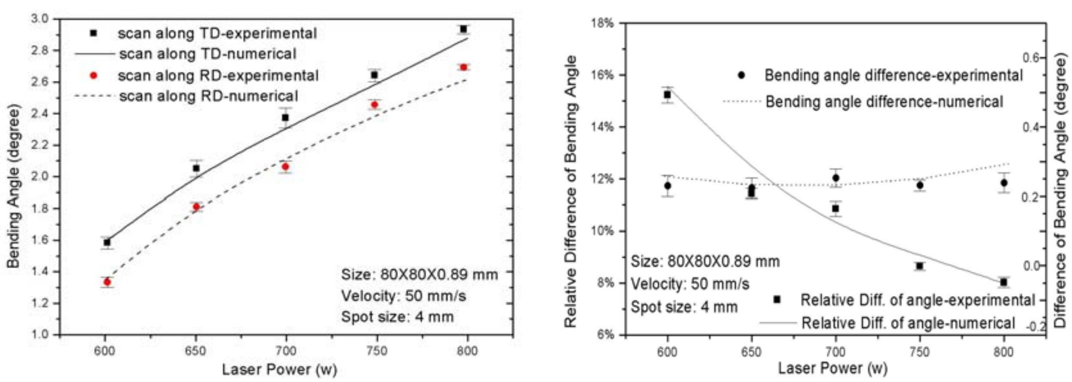

(a) (b)

Figure 10. (a) Bending angle; and (b) Differences of bending angle between scans along *RD* and *TD* (Constant speed and varying power)

5. CONCLUSIONS

The plastic anisotropy of cold-rolled mild steel sheet with different rolling reductions used in laser forming was measured in terms of *R*-values via uniaxial tensile tests; and associated textures were characterized by EBSD. The results are in agreement with that based on the texture evolution theory. Effects of the plastic anisotropy on laser forming under different conditions were experimentally and numerically investigated, and the numerical results agree with experimental ones. The anisotropic effect increases with the rolling reduction. If scanning velocity increases while laser power is kept constant, the anisotropic effect increases relative to the bending deformation, primarily due to shorter time and lower temperature for recrystallization. If the scanning velocity is kept constant while laser power increases, higher temperature will make the anisotropic effect smaller relative to the deformation.

6. REFERENCES

1. Sprenger, A., Vollertsen, F., Steen, W. F., and Watkins, K, Influence of Strain Hardening on Laser Bending. Proc. of Laser Assisted Net Shape Engg. (LANE '94). Vol. 1: 1994; pp. 361-370.
2. Li., W., and Yao, Y. L., Numerical and Experimental Study of Strain Rate Effects in Laser Forming. Journal of Manufacturing Science and Engineering. Vol. 122: 2000; pp. 445-451.
3. Kuwabara, T., and Ikeda, S., Plane-strain Tension Test of Steel Sheet using Servo-controlled Biaxial Tensile Testing Machine. J. Mater. Processing Technology. Vol. 80-81: 1998; pp. 517-523.
4. Liao, K. C., Friedman, P. A., Pan, J., and Tang, S. C., Texture Development and Plastic Anisotropy of B.C.C. Strain Hardening Sheet Metals. Int. J. Solids Structures. Vol. 35, No.36: 1998; pp. 5205-5236.
5. Hill, R., A Theory of the Yielding and Plastic Flow of Anisotropic Metals. Proceedings of the Royal Society of London, Series A, Mathematical and Physical Sciences. Vol. 193, Issue 1033: 1948; pp. 281.
6. Hosford, W. F., On the Crystallographic Basis of Yield Criteria. Textures and Microstructures. Vol. 26-27: 1996; pp. 479-493.
7. Gilormini, P., The Theory of Rate Sensitive Pencil Glide Application to Rolling Textures. Acta Metall., Vol. 37, No. 7: 1989; pp. 2093-2101.
8. Raabe, D., Simulation of Rolling Textures of b.c.c. Metals Considering Grain Interactions and Crystallographic Slip on {110}, {112} and {123} Planes. *Materials Science and Engineering*. A197: 1995; pp. 31-37.
9. Kocks, W. K., Tome, C. N., and Wenk, H. R., Texture and Anisotropy-preferred Orientations in Polycrystals and Their Effects on Materials Properties, London: Cambridge University Press, 1998.
10. Raabe, D., and Lucke, K., Rolling and Annealing Textures of BCC Metals. Materials Science Forum, Vol. 157-162: 1994; pp. 597-610.
11. Hosford, W. F., and Caddell, R. M., Metal Forming-Mechanics and Metallurgy (2nd Ed.), Prentice-Hall International, Inc., London, 1993.
12. Taylor, G. I., Plastic Strain in Metals. *J. Inst. Metals*. Vol. 62: 1938; pp. 307-324.
13. Bunge, H. J., Texture Analysis in Materials Science-Mathematical Method, Butterworths, London, 1982.
14. ASTM, Metals Test Methods and Analytical Procedures. Annual Book of ASTM Standards, Vol. 03.01: 2002.
15. Daniel, D., and Jonas, J. J., Measurement and Prediction of Plastic Anisotropy in Deep-Drawing Steels. Metallurgical Transactions A. Vol. 21A: 1990; pp. 331-343.

Meet the authors:

Peng Cheng is a Ph.D candidate in the Department of Mechanical Engineering at Columbia University. He received a BS in 1997 and a MS in 2000 in Mechanical Engineering from Tsinghua University, China. His research interest is laser forming.

Y. Lawrence Yao is a Professor in the Department of Mechanical Engineering at Columbia University. He received his Ph.D. from the University of Wisconsin-Madison in 1988. He is interested in multidisciplinary research in manufacturing and design, nontraditional manufacturing processes and laser materials processing. He serves on the Board of Directors of LIA.